ROYAL SOCIETY OF CHEMISTRY

PAPER

Check for updates

Noncentrosymmetric hybrid gallium halides built from non-polar inorganic units

Sergei A. Novikov, [a] Eric A. Gabilondo, [b] Aleksandra D. Valueva,[a] Jason Locklin [ac] and Vladislav V. Klepov *[a]

Hybrid organic–inorganic metal halide compounds are a versatile platform for developing materials for optoelectronic applications. In this report, we studied the crystal structures and optical properties of five hybrid noncentrosymmetric Ga^{3+} halides with tri- and tetraethylammonium cations. All new phases crystallize in polar space groups and contain isolated GaX_4^- units in their structures, which are charge-balanced by the corresponding organic cations. Different packing arrangements of structural units result in three distinct crystal systems for five new compounds: hexagonal, orthorhombic, and monoclinic. All new structures demonstrate SHG activity, varying from weak (0.13 × KDP) to strong (1.88 × KDP), which agrees with acentric structures of these Ga^{3+} phases. Although our attempts to relate the net dipole moments of the compounds with SHG response were unsuccessful, the coalignment of the GaX_4 tetrahedra is a likely structural prerequisite for the high SHG response observed in Et_4NGaCl_4. Overall, Ga hybrid halides provide a promising and flexible platform for the synthesis of new polar phases.

Introduction

The discovery of nonlinear optical (NLO) phenomena, such as optical harmonics generation, has broadened the spectral range of lasers, which is crucial for non-destructive studies, medicine,

*[a] Department of Chemistry, University of Georgia, Athens, Georgia, 30602, USA.
E-mail: klepov@uga.edu*
[b] Department of Chemistry, University of Houston, Houston, Texas, 77204, USA
[c] New Materials Institute, University of Georgia, Athens, Georgia, 30602, USA

Vladislav V. Klepov is an Assistant Professor in the Department of Chemistry at the University of Georgia (UGA). Prior to joining UGA, he conducted postdoctoral research at the University of South Carolina and Northwestern University. His research group studies a broad range of topics in solid state materials chemistry, including the synthesis of new quantum materials, radiation detectors, and compounds for optoelectronic applications. His

Vladislav V. Klepov

primary research goal is to elucidate the relationships between the composition and structure of new materials and their electronic and physical properties.

semiconductor deposition, and data transmission.[1–5] Noncentrosymmetric materials capable of frequency doubling (second harmonic generation, SHG) are usually divided into classes, depending on the operational spectral region: far IR and mid IR, near IR and visible, UV and deep UV.[6–9] NLO materials must transmit the light in the intendent region of application, which is defined by their bandgap values: for example, mid IR NLO materials need bandgap values above 3.0 eV, while UV NLO materials – above 6.2 eV.[5,9] Naturally, oxides have wider bandgaps compared to chalcogenides or halides, and the most common UV NLO materials are borates, carbonates, nitrates, and phosphates.[8] Particular interest in borates arises from their tendency to crystallize with noncentrosymmetric structures.[10]

Chalcogenides with more covalent bonds compared to oxides and thus lower bandgaps show promising SHG behavior in the IR region.[7] Halides with intermediate bandgaps and high transparency for IR radiation offer broad tunability of the compositions, structure, and properties to satisfy key requirements for mid-IR NLO materials.[9] One specific class of materials, hybrid organic–inorganic metal halides (and specifically halide perovskites), emerged as a tremendously versatile system covering a wide range of applications spanning from solar cells[11–13] and LEDs[14–16] to photocatalysis,[17] energy storage,[18] and medical imaging.[19,20] The flexibility of halides compositions and properties grants them a place among prospective NLO materials.[21,22]

The universal tendency of materials to crystallize in centrosymmetric space groups also applies to halides. However, hybrid halides can be endowed with noncentrosymmetric structures *via* chirality transfer from organic cations.[12,23] In a

5734 | *J. Mater. Chem. C*, 2026, **14**, 5734–5740

This journal is © The Royal Society of Chemistry 2026

direct transfer, a chiral organic cation is introduced to a metal halide structure, resulting in symmetry breaking and crystallization of material in a chiral space group.[24] Remote chirality transfer is more peculiar: here, a chirality-inducing agent is not a part of the halide structure; however, its proximity induces chirality in an otherwise non-chiral structure.[25] Both approaches employ the same organic cations.[26] Besides SHG, chiral materials demonstrate circular dichroism and circularly polarized photoluminescence.[23,27] Both inorganic metal-halide anions and organic cations of hybrid halides influence the NLO properties of a material. For example, the $(C_5H_{12}N)SnCl_3$ phase contains highly noncentrosymmetric $SnCl_3^-$ units in the structure, which are the main contributors to the SHG response of the phase.[28] On the contrary, in the $(C_7H_{10}N)PbBr_3$ phase with lead being octahedrally coordinated by bromide ions, an enhanced SHG signal is enabled *via* charge transfer from $PbBr_6^{4-}$ units to the organic cation.[29]

Chiral materials are used in enantiomer recognition and separation,[30] circularly polarized LEDs,[31] optoelectronic sensors,[32] spintronics,[33] and quantum optics.[34] Despite the compositional flexibility of halide perovskites, the practicality of their application is hindered by chemical instability issues. For example, lead halide perovskites (LHPs) decompose over time if exposed to the atmosphere and light.[35] Sn^{2+} and Ge^{2+} ions of lead-free halides are prone to oxidation to Sn^{4+} and Ge^{4+}, respectively.[36] Thus, it is practical to search for new compositions containing main group elements in stable oxidation states.[37]

In this paper, we report on the synthesis, structural, optical, and thermal characterization of five new acentric hybrid halides containing GaX_4^- anions (X = Cl, Br, or I) and tri- (Et_3NH^+) or tetraethylammonium (Et_4N^+) cations. While noncentrosymmetric structures are generally much less common compared to the centrosymmetric ones, all new phases showed a second harmonic generation signal, confirming the lack of an inversion center in their structures. As expected, the optical bandgap of a phase decreases when moving from X = Cl to I, reaching a value of 2.5 eV in Et_4NGaI_4. Interestingly, since all new phases belong to one of three polar point groups, *m*, 6*mm*, or *mm*2, they can be employed as pyroelectric and circular dichroism materials.

Results and discussion

Synthesis and crystal structures of new halides

We obtained all five materials as precipitates from aqueous solutions of HCl/HBr/HI containing Ga_2O_3 and respective organic cations (Table S1). All samples were obtained in phase pure form (Fig. 1), and no other phases were observed in these systems.

$Et_3NHGaBr_4$ and Et_3NHGaI_4 phases are isostructural and crystallize in the monoclinic polar space group *Cc* (Table 1). All atoms occupy the only 4a positions in the unit cells of Et_3NHGaX_4 (X = Br of I) phases. Each Ga atom in Et_3NHGaX_4 is surrounded by four halides in a slightly distorted tetrahedral manner, with all four Ga–X bonds being different in length as a result of C_1 (1) site symmetry (Tables S12 and S13). GaX_4 units are isolated from each other by organic cations, which also compensate for their negative charges (Fig. 2).
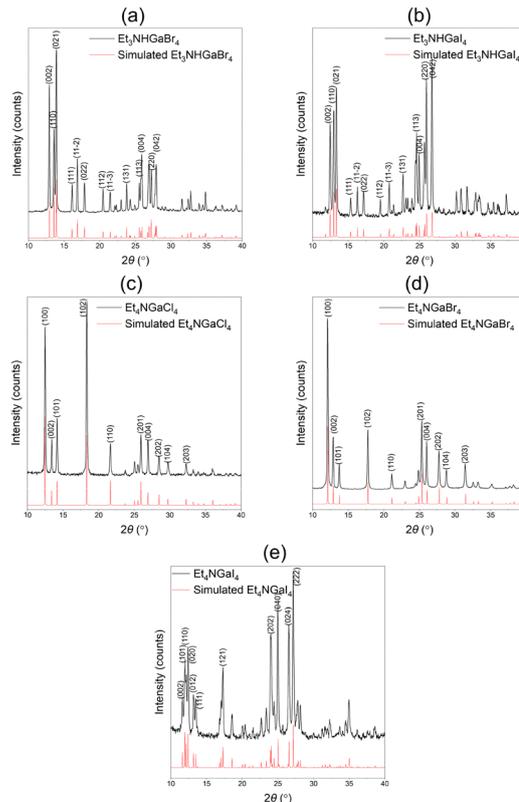

Fig. 1 Powder X-ray diffraction (PXRD) patterns of as-synthesized Et_3NH-GaX_4 (a and b) and Et_4NGaX_4 (c–e) phases overlaid with the corresponding calculated patterns.

Two Et_4NGaX_4 phases (X = Cl or Br) are isostructural and crystallize in the hexagonal polar space group $P6_3mc$ (Table 1). Ga atoms are located in the 2a positions with C_{3v} (3*m*) site symmetry. Because of this, GaX_4 tetrahedra are distorted with one bond elongated compared to three others, which are equal in length (Tables S14 and S15). The nitrogen atom of the sole tetraethylammonium cation is in the 2b position with C_{3v} (3*m*) site symmetry. Since Et_4N^+ cation is incompatible with the trifold rotation symmetry of the crystal structure, it exhibits disorder of one ethyl group. Lowering the symmetry of the structure can, in principle, resolve the disorder; however, PXRD data do not evidence lower symmetry (Fig. 1).

When a larger iodide anion is introduced to the system, the resulting Et_4NGaI_4 phase demonstrates lower symmetry compared to the chloride and bromide analogs and crystallizes in the polar orthorhombic space group $Pmn2_1$ (Table 1). Two independent Ga atoms are in 2a positions of the unit cell with C_s (*m*) site symmetry. Thus, two Ga–I bonds that are related by a mirror plane running through the GaI_4 units are equal in length, while the other two in-plane bonds have different lengths (Table S16). Tetraethylammonium cations in the structure are disordered by a mirror plane as both independent nitrogen atoms are in 2a positions in the Et_4NGaI_4 unit cell.

The average Ga–X bond length increases from 2.165(2) Å in chloride to 2.316(10) Å in bromides and 2.540(12) Å in iodides, in agreement with the increasing radius of the halide ion.

This journal is © The Royal Society of Chemistry 2026

J. Mater. Chem. C, 2026, **14**, 5734–5740 | **5735**

Table 1 Crystallographic parameters and single crystal X-ray diffraction experimental details of the new phases

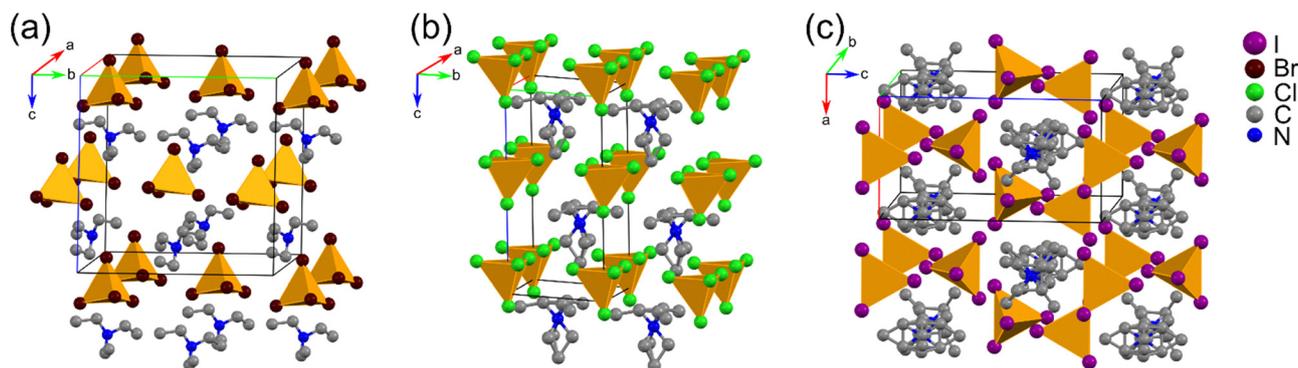| Empirical formula	$Et_3NHGaBr_4$	Et_3NHGaI_4	Et_4NGaCl_4	Et_4NGaBr_4	Et_4NGaI_4
Formula weight	475.43	663.39	321.61	499.45	687.41
Space group	Cc	Cc	$P6_3mc$	$P6_3mc$	$Pmn2_1$
a, Å	7.553(6)	7.8828(5)	8.2244(11)	8.3651(6)	8.4479(6)
b, Å	14.467(11)	15.0869(10)	8.2244(11)	8.3651(6)	14.2031(10)
c, Å	14.113(11)	14.5970(10)	13.259(3)	13.6354(13)	15.1904(12)
β, °	102.32(2)	101.596(2)	90	90	90
Volume, Å³	1507(2)	1700.5(2)	776.7(3)	826.31(14)	1822.6(2)
Z	4	4	2	2	4
ρ_{calc}, gcm⁻³	2.096	2.591	1.375	2.007	2.505
Independent reflections	3895 [R_{int} = 0.0712, R_{Sigma} = 0.0704]	4746 [R_{int} = 0.0564, R_{Sigma} = 0.0557]	833 [R_{int} = 0.1303, R_{Sigma} = 0.0510]	878 [R_{int} = 0.0914, R_{Sigma} = 0.0330]	5150 [R_{int} = 0.0973, R_{Sigma} = 0.0837]
Data/restraints/parameters	3895/15/109	4746/66/109	833/3/27	878/5/27	5150/56/117
GOOF on F²	1.047	1.003	1.102	1.124	1.020
Final R indexes [$I \geq 2\sigma (I)$]	R_1 = 0.0504, wR_2 = 0.1087	R_1 = 0.0518, wR_2 = 0.0969	R_1 = 0.0895, wR_2 = 0.2172	R_1 = 0.0517, wR_2 = 0.1335	R_1 = 0.0536, wR_2 = 0.0923
Final R indexes [all data]	R_1 = 0.1432, wR_2 = 0.1481	R_1 = 0.1215, wR_2 = 0.1166	R_1 = 0.1541, wR_2 = 0.2555	R_1 = 0.1043, wR_2 = 0.1799	R_1 = 0.1595, wR_2 = 0.1245
Largest diff. peak/hole, ēÅ⁻³	0.59/−0.61	0.69/−1.10	0.71/−0.46	0.63/−0.49	1.03/−0.87
Flack parameter	0.011(14)	0.052(18)	0.05(14)	0.01(2)	0.38(19)

Fig. 2 GaX_4 (X = Cl, Br, or I) tetrahedra and organic cations packing in (a) $Et_3NHGaBr_4$, (b) Et_4NGaCl_4 and (c) Et_4NGaI_4 structures. GaX_4 tetrahedra are orange. Organic cations are disordered in (b) and (c).

These data also agree with the acentric hybrid Ga halides deposited to CCDC[38] with average Ga–X bond lengths being 2.17(1) Å, 2.33(2) Å, and 2.55(3) Å for chlorides, bromides, and iodides, respectively. Previously reported structures also contain only isolated tetrahedral GaX_4^- units. For most of the Ga atoms in the halide surroundings, the site symmetry of their position is C_1 (1) with all four Ga–X bonds in tetrahedra having different lengths. One of the factors causing elongation of some Ga–X bonds is N–H···X hydrogen bonds between GaX_4^- tetrahedra and organic cations. The C_3 (3) site symmetry is also quite common. Other variations include C_s (m), C_{2v} ($mm2$), C_{3v} ($3m$), and S_4 (4), but are rarely presented. The X–Ga–X bond angles lie in the 104–115° range, however, despite this wide range and somewhat low site symmetry for the most Ga atoms, the average X–Ga–X bond angle is 109.47(1)°, which corresponds to the near ideal tetrahedral coordination.

Optical properties

All new phases crystallize in the polar space groups and thus should demonstrate piezoelectric and NLO properties.[39] SHG data collected for new halides confirm that all phases are acentric (Fig. 3 and Table S22). The highest SHG response

(1.88 × KDP, Fig. 3) was found in the Et_4NGaCl_4 phase, while the Et_4NGaI_4 phase demonstrates the lowest SHG intensity among the five samples (0.13 × KDP). SHG activities of three other phases are slightly higher than for KDP (Fig. 3 and Table S22).

As can be seen from the SHG data, the new phases exhibit significantly different NLO activity, which, however, does not align with the expected trends. One would anticipate that compounds with more polarizable bonds, i.e., those containing heavier halide anions, would demonstrate higher SHG response. Contrary to this expectation, Et_4NGaI_4 exhibits the lowest SHG response. One possible reason for that is the reabsorption of the double-frequency light by the material. To evaluate this effect, we collected their UV-vis spectra and calculated band gaps of the materials assuming direct bandgaps (Fig. S1). As expected, the iodides, which demonstrate darker colors, have lower bandgaps, 2.5 eV for Et_4NGaI_4 and 2.8 eV for Et_3NHGaI_4. Although the 532 nm second harmonic of the YAG:Nd laser corresponds to a slightly lower energy, ≈2.33 eV, the UV-vis spectra of both compounds exhibit absorption tails in the lower energy region, which likely arise from defect states. Due to the reabsorption, both compounds show either low (Et_4NGaI_4, 0.13 × KDP) or moderate (Et_3NHGaI_4, 1.07 × KDP) SHG responses. To avoid

5736 | J. Mater. Chem. C, 2026, **14**, 5734–5740

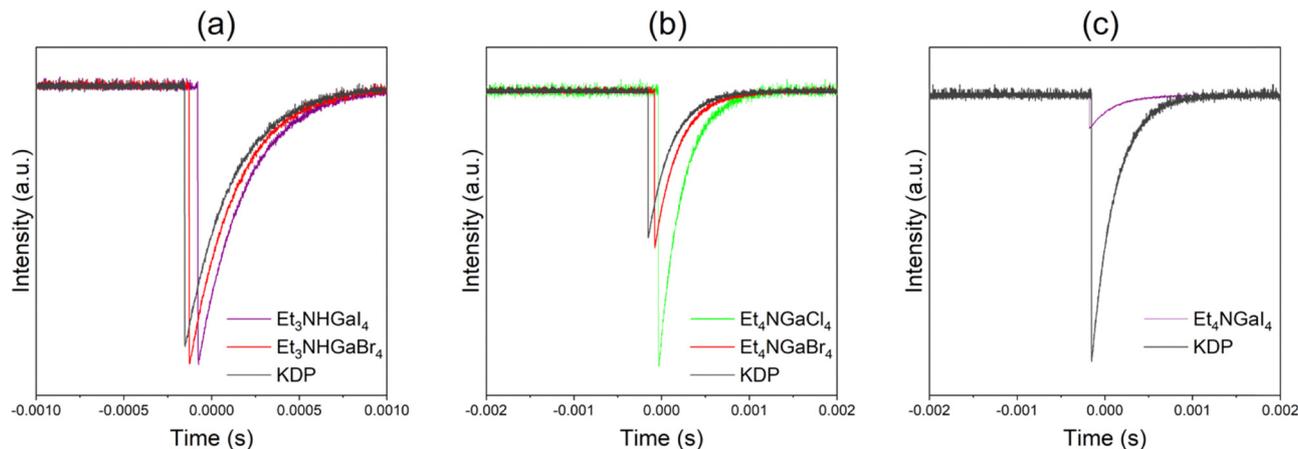This journal is © The Royal Society of Chemistry 2026

Fig. 3 SHG signal intensity in new Ga hybrid halides and KDP standard sample at 1064 nm.

reabsorption effects, both iodides were also studied with 2090 nm IR laser against AgGaS$_2$ (AGS) standard. The activity of Et$_3$NHGaI$_4$ was moderate (1.65 × AGS), while no SHG signal was detected from the tetraethylammonium phase (Fig. S2).

The remaining three compounds with bromide and chloride anions have wider bandgaps (> 4 eV, Fig. S1) according to UV-vis data and should be transparent for the double frequency SHG response. However, even isostructural Et$_4$NGaCl$_4$ and Et$_4$NGaBr$_4$ counter the expected trend of increasing SHG response upon heavier halide atom incorporation. One of the factors contributing to the difference is the alignment of the GaX$_4$ tetrahedra net dipole moments in the structures of new phases. To calculate the dipole moments of Ga–X bonds and the total net dipole moments, we used the approach previously employed by *Choi et. al.* for ZnCl$_4$ units.[40] For isostructural Et$_4$NGaX$_4$ (X = Cl and Br) phases, the net dipole moments are coaligned along one of the Ga–X bonds of the tetrahedra and the *c* axis of the unit cell (Fig. S3). The net dipole moment of a GaCl$_4$ tetrahedron is half that of the GaBr$_4$ one (Table S23), which is in agreement with the expected trend, but contradicts the higher SHG response in the Et$_4$NGaCl$_4$ phase. It is therefore likely that other factors, such as birefringence and phase-matching, play a more important role. We collected phase-matching data for Et$_4$NGaCl$_4$ that demonstrated the highest SHG response among the phases reported here (Fig. S4). We found that the SHG response significantly decreases as the particle size increases, showing that this sample is not phase matchable.

NLO materials based on acentric Ga^{3+} hybrid halides were not extensively studied to date, as these phases commonly form as side products in the synthesis of galloorganic molecules. Out of all acentric hybrid chlorides, bromides, and iodides of Ga^{3+} deposited in CCDC, SHG activity was only reported for the Me$_4$NGaCl$_4$ phase (Me = –CH$_3$).[41] This tetramethylammonium phase demonstrates a higher activity (2.5 × KDP) compared to the ethylammonium analog. In the Me$_4$NGaCl$_4$ structure, site symmetry on Ga atoms is C$_{2v}$ (*mm*2), which does not match the symmetry of the GaX$_4^-$ units in our phases. The dipole moments of individual Ga–Cl bonds are comparable to those in the Et$_4$NGaCl$_4$ phase (≈16.7 D), however the net dipole moments

of GaCl$_4^-$ tetrahedra are six times higher (Table S23). Moreover, unlike in Et$_3$NHGaBr$_4$ and Et$_4$NGaI$_4$ phases with similar magnitude of net dipole moments, in Me$_4$NGaCl$_4$ they are also coaligned along the same axis, which explains the higher NLO activity of this material.

Thermal behavior

As structural units of the phases under consideration show only weak interactions, these materials can be candidates for ionic liquids. To study the thermal behavior of new phases, we collected DSC data. DSC study of the Et$_4$NGaI$_4$ sample revealed two endo effects followed by one exo effect upon the first heating cycle (Fig. 4). Further cooling and heating curves do not demonstrate any features, suggesting that Et$_4$NGaI$_4$ phase undergoes irreversible phase transition or partial decomposition. Since thermogravimetric analysis (TGA) shows no significant weight loss in the 30–150 °C temperature range, no gaseous products should form in the decomposition process (Fig. 4). Complete decomposition of the sample observed above 400 °C (Fig. S5). PXRD study of the Et$_4$NGaI$_4$ sample after DSC revealed that a new phase (or phases) formed during temperature treatment of the Et$_4$NGaI$_4$ sample (Fig. S5). The new phase was indexed from the experimental PXRD data as an orthorhombic one, *Pmmm* space group, *a* = 4.3428(5) Å, *b* = 7.5295(6) Å, and *c* = 14.3868(8) Å (Fig. S5), but no apparent matches of the refined unit cell parameters with reported structures containing the corresponding elements were found.

Unlike Et$_4$NGaI$_4$, Et$_4$NGaBr$_4$ does not melt or undergo a phase transition up to 150 °C (Fig. S6). Et$_3$NHGaI$_4$ and Et$_4$NGaCl$_4$ melt above 100 °C and do not show notable supercooling (Fig. S6). Finally, the Et$_3$NHGaBr$_4$ phase appears to react with the aluminum DSC pan, resulting in unreliable melting temperatures for this phase. PXRD data collected from Et$_3$NHGaI$_4$, Et$_4$NGaCl$_4$, and Et$_4$NGaBr$_4$ samples after DSC confirm their stability upon heating disregarding the presence of thermal effects (Fig. S7). Moreover, unlike many hybrid phases containing Pb^{2+}, Ge^{2+}, or Sn^{2+}, these materials showed long term stability. Samples stored for 5 months on a shelf did not show deterioration in crystallinity, nor did new peaks appear in the PXRD patterns (Fig. S8).
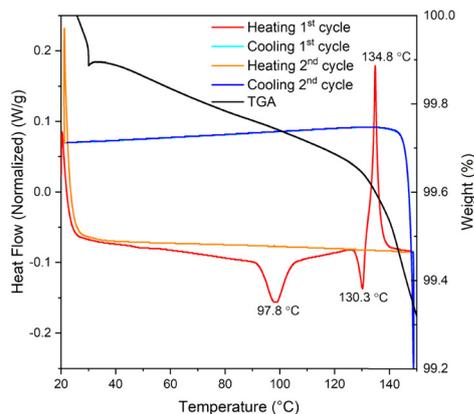
This journal is © The Royal Society of Chemistry 2026

J. Mater. Chem. C, 2026, **14**, 5734–5740 | **5737**

Fig. 4 DSC-TGA study of Et_4NGaI_4 sample. Peaks positions are shown in the figure. No significant sample weight loss was detected in TGA analysis.

Conclusion

Five acentric gallium hybrid halides were synthesized and their structures, linear and nonlinear optical properties, and thermal behavior were characterized. Surprisingly, all new phases crystallized in polar space groups, even though no polarity inducing agents were introduced in the synthesis. In all the new phases, Ga atoms demonstrate exclusively tetrahedral coordination to halides. The resulting tetrahedra are distorted, as the site symmetries of Ga positions are lower than T_d. One of the phases, Et_4NGaCl_4, demonstrates promising NLO activity ($1.88 \times$ KDP) and can be easily prepared on a large scale, showing that Ga^{3+} hybrid halides can be a versatile platform for the preparation of new NLO materials. Two phases, Et_3NHGaI_4 and Et_4NGaCl_4, melt above 100 °C offering another platform for high-temperature reaction media.

Experimental

Synthesis

Initial reagents for the synthesis of new halide phases were Ga_2O_3 (99.9%), triethylamine (Et_3N, 99%), tetraethylammonium chloride (Et_4NCl, 99.4%), tetraethylammonium bromide (Et_4NBr, 99%), and concentrated HX acids (X = Cl, Br, or I). First, calculated amounts of Ga_2O_3 were weighed and dissolved in excess of the corresponding acid (Table S1). For the synthesis of iodides, small portions of H_3PO_2 were added to the reaction to prevent iodide anion oxidation. Triethylamine was added on stirring directly to the acidic solutions containing Ga^{3+} ions. Tetraethylammonium halides were dissolved in HX separately and then added to the Ga^{3+} solutions. For all systems, mixing of reagents caused immediate precipitation. Precipitates used for properties measurements were separated from solutions by vacuum filtration on a glass filter. Small portions of precipitates were used for recrystallization of target phases to obtain crystals suitable for a single crystal X-ray diffraction study (Table S1).

Characterization

Single crystal X-ray diffraction was used to determine the structures of new phases (Tables S2–S21). Room temperature

data sets were collected on Bruker D8 QUEST diffractometer (Mo Kα radiation, λ = 0.71073 Å) equipped with hybrid photon counting area detector. Raw data were integrated with Saint-PLUS software.[42] Correction for absorption was performed with SADASBS program.[43] Structures of all new compound were solved by the intrinsic phasing method with SHELXT software,[44] and refined against F^2 with SHELXL program[45] using Olex2 interface.[46]

Phase purity of the samples was tested with PXRD on a Bruker D2 Phaser instrument (Cu anode) equipped with LYNXEYE energy dispersive 1D detector. Indexing of the unknown product formed upon heating of the Et_4NGaI_4 sample was done with GSAS-II.[47] LeBail fitting was performed in Rietica software.[48]

A modified Kurtz–Perry system[49,50] equipped with a 1064 nm Nd:YAG and 2090 nm Ho:YAG lasers was used to collect powder SHG data. KH_2PO_4 (KDP) and $AgGaS_2$ (AGS) served as the references for the samples studied with a 1064 nm and 2090 nm lasers respectively.

Defuse reflectance spectra were collected on a Shimadzu UV-2450 (Kyoto, Japan) spectrometer and an Edinburgh Instruments FS5 Spectrofluorometer equipped with an integrating sphere at room temperature in the 200–800 nm wavelength range. $BaSO_4$ was employed as a non-absorbing reflectance reference for calibration. Iodides were ground with excess $BaSO_4$ before the measurements.

Thermal transitions were evaluated using a TA Discovery 250 differential scanning calorimeter (TA Instruments, New Castle, Delaware, USA) under nitrogen. The samples (10–20 mg) were enclosed in aluminum pans before testing. After equilibrating at 20 °C, samples were heated to 150 °C at a heating rate of 5 °C min^{-1} and subsequently cooled to 20 °C at a rate of 5° min^{-1}. Two of these heating and cooling cycles were employed. Thermogravimetric analysis (TGA) of samples was conducted using a TA Instruments Discovery TGA 550. The samples (7–14 mg) were heated from 20 °C to 900 °C at 10 °C min^{-1} rate.

Conflicts of interest

There are no conflicts to declare.

Data availability

The data supporting this article have been included as part of the supplementary information (SI). Supplementary information: synthesis procedures, crystallographic data, SHG data, Tauc plots, dipole moments, PXRD study of the samples, DSC and TGA data. See DOI: https://doi.org/10.1039/d5tc03829d.

CCDC 2492463–2492467 contain the supplementary crystallographic data for this paper.[51a–e]

Acknowledgements

5738 | *J. Mater. Chem. C*, 2026, **14**, 5734–5740

This journal is © The Royal Society of Chemistry 2026

Notes and references

1 D. Cotter, R. J. Manning, K. J. Blow, A. D. Ellis, A. E. Kelly, D. Nesset, I. D. Phillips, A. J. Poustie and D. C. Rogers, *Science*, 1999, **286**, 1523–1528.

2 J. Guck, R. Ananthakrishnan, H. Mahmood, T. J. Moon, C. C. Cunningham and J. Käs, *Biophys. J.*, 2001, **81**, 767–784.

3 G. Cerullo and S. De Silvestri, *Rev. Sci. Instrum.*, 2003, **74**, 1–18.

4 D. T. Spencer, T. Drake, T. C. Briles, J. Stone, L. C. Sinclair, C. Fredrick, Q. Li, D. Westly, B. R. Ilic, A. Bluestone, N. Volet, T. Komljenovic, L. Chang, S. H. Lee, D. Y. Oh, M.-G. Suh, K. Y. Yang, M. H. P. Pfeiffer, T. J. Kippenberg, E. Norberg, L. Theogarajan, K. Vahala, N. R. Newbury, K. Srinivasan, J. E. Bowers, S. A. Diddams and S. B. Papp, *Nature*, 2018, **557**, 81–85.

5 H. Z. Aslam, J. T. Doane, M. T. Yeung and G. Akopov, *ACS Appl. Opt. Mater.*, 2023, **1**, 1898–1921.

6 Y. Xia, C. Chen, D. Tang and B. Wu, *Adv. Mater.*, 1995, **7**, 79–81.

7 I. Chung and M. G. Kanatzidis, *Chem. Mater.*, 2014, **26**, 849–869.

8 T. T. Tran, H. Yu, J. M. Rondinelli, K. R. Poeppelmeier and P. S. Halasyamani, *Chem. Mater.*, 2016, **28**, 5238–5258.

9 P. Gong, F. Liang, L. Kang, X. Chen, J. Qin, Y. Wu and Z. Lin, *Coord. Chem. Rev.*, 2019, **380**, 83–102.

10 P. Becker, *Adv. Mater.*, 1998, **10**, 979–992.

11 T. Baikie, Y. Fang, J. M. Kadro, M. Schreyer, F. Wei, S. G. Mhaisalkar, M. Graetzel and T. J. White, *J. Mater. Chem. A*, 2013, **1**, 5628–5641.

12 L. Mao, J. Chen, P. Vishnoi and A. K. Cheetham, *Acc. Mater. Res.*, 2022, **3**, 439–448.

13 H.-S. Kim, C.-R. Lee, J.-H. Im, K.-B. Lee, T. Moehl, A. Marchioro, S.-J. Moon, R. Humphry-Baker, J.-H. Yum, J. E. Moser, M. Grätzel and N.-G. Park, *Sci. Rep.*, 2012, **2**, 591.

14 W. Deng, T. Fan, X. Wu, J. Lü, W. Fan, T. Deng and H. He, *Ceram. Int.*, 2022, **48**, 29991–29996.

15 G. H. Lee, K. Kim, Y. Kim, J. Yang and M. K. Choi, *Nano-Micro Lett.*, 2023, **16**, 45.

16 S. A. Novikov, A. D. Valueva and V. V. Klepov, *Dalton Trans.*, 2024, **53**, 12442–12449.

17 J. Lee, S.-P. Chai and L.-L. Tan, *ACS Energy Lett.*, 2024, **9**, 1932–1975.

18 A. Gaurav, A. Das, A. Paul, A. Jain, B. D. Boruah and M. Abdi-Jalebi, *J. Energy Storage*, 2024, **88**, 111468.

19 T. Feng, Z. Zhou, Y. An, L. Chen, Y. Fu, S. Zhou, N. Wang, J. Zheng and C. Sun, *ACS Nano*, 2024, **18**, 16715–16725.

20 R. Liu, F. Li, F. Zeng, R. Zhao and R. Zheng, *Appl. Phys. Rev*, 2024, **11**, 021327.

21 J. Xu, X. Li, J. Xiong, C. Yuan, S. Semin, T. Rasing and X.-H. Bu, *Adv. Mater.*, 2020, **32**, 1806736.

22 G. Laurita and R. Seshadri, *Acc. Chem. Res.*, 2022, **55**, 1004–1014.

23 J. Ma, C. Fang, C. Chen, L. Jin, J. Wang, S. Wang, J. Tang and D. Li, *ACS Nano*, 2019, **13**, 3659–3665.

24 M. K. Jana, R. Song, H. Liu, D. R. Khanal, S. M. Janke, R. Zhao, C. Liu, Z. Valy Vardeny, V. Blum and D. B. Mitzi, *Nat. Commun.*, 2020, **11**, 4699.

25 M. A. Haque, A. Grieder, S. P. Harvey, R. Brunecky, J. Y. Ye, B. Addison, J. Zhang, Y. Dong, Y. Xie, M. P. Hautzinger, H. H. Walpitage, K. Zhu, J. L. Blackburn, Z. V. Vardeny, D. B. Mitzi, J. J. Berry, S. R. Marder, Y. Ping, M. C. Beard and J. M. Luther, *Nat. Chem.*, 2025, **17**, 29–37.

26 J. Guan, W. Han, Y. Zhang, J. Zhao, S. Han, Y. Wang, B. Fu, H. Kang, P. Wang, P. Cheng, Y. Zheng, J. Xu and X.-H. Bu, *Angew. Chem., Int. Ed.*, 2025, e202503083.

27 S. Ma, J. Ahn and J. Moon, *Adv. Mater.*, 2021, **33**, 2005760.

28 X. Liu, C. Ji, Z. Wu, L. Li, S. Han, Y. Wang, Z. Sun and J. Luo, *Chem. – Eur. J.*, 2019, **25**, 2610–2615.

29 P. Cheng, X. Jia, S. Chai, G. Li, M. Xin, J. Guan, X. Han, W. Han, S. Zeng, Y. Zheng, J. Xu and X.-H. Bu, *Angew. Chem., Int. Ed.*, 2024, **63**, e202400644.

30 A. Gogoi, N. Mazumder, S. Konwer, H. Ranawat, N.-T. Chen and G.-Y. Zhuo, *Molecules*, 2019, **24**, 1007.

31 J. Lu, B. Shao, R.-W. Huang, L. Gutiérrez-Arzaluz, S. Chen, Z. Han, J. Yin, H. Zhu, S. Dayneko, M. N. Hedhili, X. Song, P. Yuan, C. Dong, R. Zhou, M. I. Saidaminov, S.-Q. Zang, O. F. Mohammed and O. M. Bakr, *J. Am. Chem. Soc.*, 2024, **146**, 4144–4152.

32 J. Ahn, S. H. Lee, I. Song, P. Chidchob, Y. Kwon and J. H. Oh, *Device*, 2023, **1**, 100176.

33 S.-H. Yang, R. Naaman, Y. Paltiel and S. S. P. Parkin, *Nat. Rev. Phys.*, 2021, **3**, 328–343.

34 S. Barik, A. Karasahin, S. Mittal, E. Waks and M. Hafezi, *Phys. Rev. B*, 2020, **101**, 205303.

35 G. P. Nagabhushana, R. Shivaramaiah and A. Navrotsky, *Proc. Natl. Acad. Sci. U. S. A.*, 2016, **113**, 7717–7721.

36 F. Giustino and H. J. Snaith, *ACS Energy Lett.*, 2016, **1**, 1233–1240.

37 A. D. Valueva, S. A. Novikov, E. Gabilondo, H. B. Tisdale, A. A. Maksimova, M. Parker, V. Reukov and V. V. Klepov, *ACS Mater. Lett.*, 2025, **7**(8), 2814–2821.

38 C. R. Groom, I. J. Bruno, M. P. Lightfoot and S. C. Ward, *Acta Crystallogr., Sect. B: Struct. Sci., Cryst. Eng. Mater.*, 2016, **72**, 171–179.

39 P. S. Halasyamani and K. R. Poeppelmeier, *Chem. Mater.*, 1998, **10**, 2753–2769.

40 M.-H. Choi, S.-H. Kim, H.-Y. Chang, P. S. Halasyamani and K. M. Ok, *Inorg. Chem.*, 2009, **48**, 8376–8382.

41 D. Li, X.-M. Zhao, H.-X. Zhao, X.-W. Dong, L.-S. Long and L.-S. Zheng, *Adv. Mater.*, 2018, **30**, 1803716.

42 *SAINT-Plus (Version 7.68)*, Bruker AXS Inc., Madison, Wisconsin, USA, 2007.

43 *SADABS*, Bruker AXS Inc., Madison, Wisconsin, USA, 2008.

44 G. M. Sheldrick, *Acta Crystallogr., Sect. A: Found. Adv.*, 2015, **71**, 3–8.

45 G. M. Sheldrick, *Acta Crystallogr., Sect. C: Struct. Chem.*, 2015, **71**, 3–8.

46 O. V. Dolomanov, L. J. Bourhis, R. J. Gildea, J. A. K. Howard and H. Puschmann, *J. Appl. Crystallogr.*, 2009, **42**, 339–341.

47 B. H. Toby and R. B. Von Dreele, *J. Appl. Crystallogr.*, 2013, **46**, 544–549.

48 B. Hunter, *International Union of Crystallography Commission on Powder Diffraction Newsletter*, 1998.

This journal is © The Royal Society of Chemistry 2026

J. Mater. Chem. C, 2026, **14**, 5734–5740 | **5739**

49 S. K. Kurtz and T. T. Perry, *J. Appl. Phys.*, 1968, **39**, 3798–3813.

50 J. P. Dougherty and S. K. Kurtz, *J. Appl. Crystallogr.*, 1976, **9**, 145–158.

51 (*a*) CCDC 2492463: Experimental Crystal Structure Determination, 2026, DOI: 10.5517/ccdc.csd.cc2pnm11; (*b*) CCDC 2492464: Experimental Crystal Structure Determination, 2026, DOI: 10.5517/ccdc.csd.cc2pnm22; (*c*) CCDC 2492465: Experimental Crystal Structure Determination, 2026, DOI: 10.5517/ccdc.csd.cc2pnm33; (*d*) CCDC 2492466: Experimental Crystal Structure Determination, 2026, DOI: 10.5517/ccdc.csd.cc2pnm44; (*e*) CCDC 2492467: Experimental Crystal Structure Determination, 2026, DOI: 10.5517/ccdc.csd.cc2pnm55.

5740 | *J. Mater. Chem. C*, 2026, **14**, 5734–5740

This journal is © The Royal Society of Chemistry 2026